RSC Advances

PAPER

Cite this: *RSC Adv.*, 2023, **13**, 906

Regeneration of NCM622 from end-of-life lithium-ion battery cathode materials†

Shuai Gu, *[ab] Ting He,[ab] Jiao Kong,[ab] Tongtong Fu,[c] Zirui Guo,[c] Jingzhi Cui[c] and Zhihao Chen[c]

Received 2nd November 2022
Accepted 19th December 2022

DOI: 10.1039/d2ra06937g

rsc.li/rsc-advances

The boom of the electric vehicle industry significantly aggravates the demand for lithium-ion batteries (LIBs), especially the ternary cathode materials, however, the majority of end-of-life (EOL) LIBs on the market are batteries utilized in customer electronics. Here, we utilized the mixed EOL LIBs from cell phones and laptops to manufacture the $LiNi_{0.6}Co0._2Mn_{0.2}O_2$ (NCM622) cathode material. A feasible, high efficiency (99.98% Co, 99.98% Ni, 99.99% Mn, and 99.99% Li), and ultra-fast leaching of EOL LIB cathodes was achieved. Thermodynamic calculations suggested that the coordination number, coordination species concentrations, and fractions have significant effects on the apparent activation energy and the equilibrium of the leaching reactions. The remanufactured NCM622 cathode material demonstrated a well-ordered layered hexagonal structure with a low Li^+/Ni^{2+} mixing ratio, which facilitated reliable reversible capacity, low polarization, high rate capabilities (163.8 mA h g^{-1}), and capacity retention ratio (94.3%).

In the last decade, the lithium-ion battery (LIB) market has been growing at an extraordinary pace and will continue to grow at no less than the same pace over the decades to come. However, the wide utilization of LIBs is a double-edged sword. According to estimation, the end-of-life (EOL) LIBs in China alone constituted 50 metric tons in 2020.[1] The enormous amount of EOL LIBs could pose serious threats to both the environment and human health by explosions and contamination of soil and groundwater if handled improperly. What's more, the manufacturing process of LIBs requires an enormous amount of nonrenewable strategic metals,[2,3] *i.e.*, Co, Ni, Mn, and Li. Thus, the recycling of EOL LIBs is both imperative and profitable, since it not only eliminates potential environmental and ecological risks but also secures the supply of precious strategic metals.[4] Numerous researches had been done on the recycling or remanufacturing of power LIBs.[5–7] However, according to circular energy storage's report, LIBs utilized in portable devices account for 80% of the total EOL LIBs for recycling in the year 2019, since more than 90% of power batteries went through cascade utilization process before being recycled. Here, we recycled the typical EOL LIBs utilized in portable devices, especially mobile phones and laptops, and remanufactured $LiNi_{0.6}Co_{0.2}Mn_{0.2}O_2$ (NCM622) cathode material from the leaching solution for the production of power batteries. Leaching, as the most reagents and time-consuming step among the recycling process, is studied in detail here. Various combinations of reductant agents and acids were proposed and studied for the efficient leaching of strategic metals from LIBs cathode materials, *i.e.*, inorganic acids,[8] organic acids,[9] inorganic acids with inorganic reductants,[10–12] inorganic acids with organic reductants,[13] organic acids with inorganic reductants,[14–16] organic acids with organic reductants,[17–21] among those the combinations of inorganic acids with organic reductants exhibited the fastest leaching kinetics. In our previous study, the ultra-fast leaching of EOL LIBs has been achieved in the HCl-ascorbic acid (VC)[4,22] and the HNO_3-VC system,[23] however, the utilization of a large amount of expensive VC weakened their industrial application potential. Considering this, mixed acids, *i.e.*, HCl, HNO_3, and VC, are adopted here for more feasible recycling of EOL LIBs cathode materials. Also, to shed light on the recycling mechanism in all steps, thermodynamic calculations were carried out.

Materials and methods

EOL LIBs were collected from laptops and cell phones, and then manually disassembled, dissolved in NMP, ultrasonically peeled, dried, and calcined to obtain a cathode material powder as shown in Fig. S1 in the ESI.† All materials used in the experiment are shown in ESI†. The closed-loop hydrometallurgy

[a]National Engineering Research Center for Integrated Utilization of Salt Lake Resources, East China University of Science and Technology, Shanghai, 200237, China. E-mail: gushuai@ecust.edu.cn

[b]Joint International Laboratory for Potassium and Lithium Strategic Resources, East China University of Science and Technology, Shanghai, 200237, China

[c]School of Chemical Engineering, East China University of Science and Technology, Shanghai 200237, China

† Electronic supplementary information (ESI) available. See DOI: https://doi.org/10.1039/d2ra06937g

process for the recycling of EOL LIBs cathode materials was divided into three steps as shown in Scheme 1:

Step 1: Leaching and removing impurity.

The collected mixed cathode material was first dissolved in the mixed acids. The mixed acids (HCl: 0, 0.25, 0.5, 0.75, and 1 M; HNO_3: 0, 0.25, 0.5, 0.75, and 1 M; VC: 0, 0.25, 0.5, 0.75, and 1 M), leaching temperature (30, 50, 70, 90 °C), solid–liquid ratio (5, 10, 20, 40 g L^{-1}), and leaching time (1, 3, 5, 7, 9, 11, 15, 20, 30, 40 min) were studied in detail to optimize the leaching conditions. The total concentration of mixed acids was kept at 1 M to reduce reagents' consumption. The effluent then went through a neutralization process with 1 M NH_4OH until the pH reaches 5.5, during which process, the majority of Al^{3+} would precipitate as $Al(OH)_3$. The optimum ending pH was determined by both thermodynamic calculations and experimental results. Afterward, the precipitate was filtered out of the effluent with a 0.25 μm membrane filter.

Step 2: Precipitation of NCM622 precursor and remanufacturing of NCM622 cathode material.

The concentrations of Ni, Co, and Mn in the effluent were measured and adjusted with extra $NiCl_2$ and $MnCl_2$ until the mole ratios of Ni : Co : Mn = 6 : 2 : 2 as the raw material for the synthesis of NCM622 precursor ($Ni_{0.6}Co_{0.2}Mn_{0.2}CO_3$). An excessive amount of Na_2CO_3 was added to precipitate the NCM622 precursor and the precipitation pH was maintained by adding 1 M NH_4OH during the process. The precipitation solution was stirred at 700 rpm and aged for 1 h before filtration in a glass Buchner funnel with a 0.25 μm membrane filter. The filtered NCM622 precursor was repeatedly washed with deionized water until the conductivity of the filtrate was less than 30 μs cm^{-1}. After vacuum drying at 80 °C for 24 h, then the filtered NCM622 precursor was mixed with Li_2CO_3 at a Li/M (M is the sum of transition metals Ni, Co, Mn) molar ratio of 1.06. Finally, the mixture was calcinated with a tube furnace (Nabertherm, RHTC 80-230/15) at 800 °C for 12 h under the atmosphere of pure O_2 gas to obtain NCM622. The as-recovered powder was then analyzed with XRD and SEM-EDX. The electrochemical properties were measured in a CR2025 coin type cell with Li foil serving as the anode electrode. The cathode was prepared with the active materials, polyvinylidene fluoride (PVDF) (weight ratio of 8 : 1 : 1) solved in *N*-methyl-2-pyrrolidone (NMP). The NCM622 cathode material was coated onto an Al foil and dried under a vacuum at 120 °C for 12 h. The cell was assembled in an argon-filled glovebox. The galvanostatic charge and discharge test was carried out at 25 °C between 2.7 and 4.3 V. The rate performance test was carried out by using the current density of 0.2C, 0.5C, 1C, 2C, 5C and 0.2C to charge and discharge the samples for 5 cycles. The cyclic voltammetry (CV) was tested with a voltage range from 2.7 to 4.3 V, scan rate 0.1 mV s^{-1}, three cycles. All electrochemical properties tests were performed in an electrochemical workstation (CorrTest, CS310M).

Step 3: Precipitation of Li_2CO_3.

After the precipitation of Al^{3+} and NCM622 precursor, Li content has a certain amount of loss. In addition, due to the intrinsic solubility of Li_2CO_3 (1.32 g per 100 mL at 293 K), the concentration of Li^+ in the effluent was too low, which is not conducive to the effective precipitation of Li_2CO_3. As a result, the effluent was first concentrated 10 times by rotary evaporation, then an excessive amount of Na_2CO_3 was added to precipitated Li_2CO_3. The precipitate was also filtered and dried at 80 °C for 24 h. And the recovered Li_2CO_3 can be utilized in Step 2 for the manufacturing of NCM 622 cathode material.

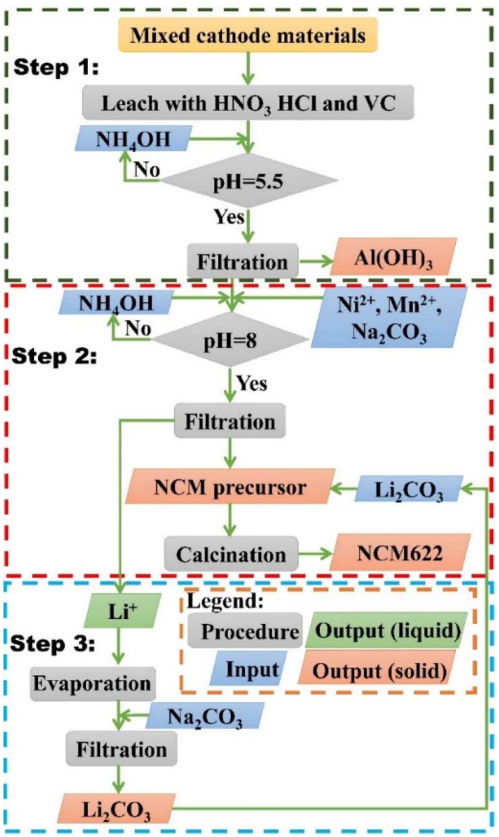

Scheme 1 A closed-loop recycling process of EOL LIBs cathode materials.

Calculation

Correlations and significances. The correlations and significances between mixed acids ratios and leaching efficiencies were evaluated by the Pearson correlation coefficient (PCC) and significance calculated by IBM SPSS.

Thermodynamic calculations. Thermodynamic calculations were utilized to determine the experimental range and reveal the mechanism in the leaching, impurity removing, and NCM622 remanufacturing process. All possible species of Co, Ni, Mn, Li, and Al in aqueous and solid phases, the corresponding reactions, and thermodynamic parameters were first collected from previously published papers and HSC Chemistry 10.1 database.[24–26] To reveal the efficient leaching mechanism, the Co complexes species,[27–29] *i.e.*, $CoCl^+$, $CoCl_2$, $CoCl_3^-$, $CoCl_4^{2-}$, $CoNO_3^+$ and $CoNO_2^+$, the Ni complexes species,[30] *i.e.*, $NiCl^+$, $NiCl_2$, $NiCl_3^-$, $NiCl_4^{2-}$, $NiNO_3^+$ and $NiNO_2^+$, and the Mn complexes species,[31] *i.e.*, $MnCl^+$, $MnCl_2$, $MnCl_3^-$, $MnCl_4^{2-}$, $MnNO_3^+$ and $MnNO_2^+$ was taken into consideration and the corresponding chemical reactions were shown in eqn (1)–(9).

$$Co^{2+} + nCl^- \leftrightarrow CoCl_n^{2-n} \log \beta_{Co}{}^n \Delta G_{Co}{}^n = -RT \ln \beta_{Co}{}^n \quad (1)$$

$$Co^{2+} + NO_3^- \leftrightarrow CoNO_3^+ \log K_{Co}^a \Delta G_{Co}^a = -RT \ln K_{Co}^a \quad (2)$$

$$Co^{2+} + NO_2^- \leftrightarrow CoNO_2^+ \log KCob \Delta G_{Co}^b = -RT \ln K_{Co}^b \quad (3)$$

$$Ni^{2+} + nCl^- \leftrightarrow NiCl_n^{2-n} \log \beta_{Ni}{}^n \Delta G_{Ni}{}^n = -RT \ln \beta_{Ni}{}^n \quad (4)$$

$$Ni^{2+} + NO_3^- \leftrightarrow NiNO_3^+ \log K_{Ni}^a \Delta G_{Ni}^a = -RT \ln K_{Ni}^a \quad (5)$$

$$Ni^{2+} + NO_2^- \leftrightarrow NiNO_2^+ \log K_{Ni}^b \Delta G_{Ni}^b = -RT \ln K_{Ni}^b \quad (6)$$

$$Mn^{2+} + nCl^- \leftrightarrow MnCl_n^{2-n} \log \beta_{Mn}{}^n \Delta G_{Mn}{}^n = -RT \ln \beta_{Mn}{}^n \quad (7)$$

$$Mn^{2+} + NO_3^- \leftrightarrow MnNO_3^+ \log K_{Mn}^a \Delta G_{Mn}{}^1 = -RT \ln K_{Mn}^a \quad (8)$$

$$Mn^{2+} + NO_2^- \leftrightarrow MnNO_2^+ \log K_{Mn}^b \Delta G_{Mn}{}^2 = -RT \ln K_{Mn}^b \quad (9)$$

where $\beta_{Co}{}^n$ ($n = 1, 2, 3, 4$) represents the accumulative stability constants of Co coordination with chloride ions, $\beta_{Ni}{}^n$ ($n = 1, 2, 3, 4$) is the accumulative stability constants of Ni coordination with chloride ions, $\beta_{Mn}{}^n$ ($n = 1, 2, 3, 4$) is the accumulative stability constants of Mn coordination with chloride ions, K_{Co}^a is the stability constants of Co complex with nitrate ion, K_{Co}^b is the stability constants of Co complex with nitrite ion, K_{Ni}^a is the stability constants of Ni complex with nitrate ion, K_{Ni}^b is the stability constants of Ni complex with nitrite ion, K_{Mn}^a is the stability constants of Mn complex with nitrate ion, K_{Mn}^b is the stability constants of Mn complex with nitrite ion, ΔG is the Gibbs free energy change in kJ mol^{-1}, R is gas constant, T is the absolute temperature in K. In the experimental temperature and pH range, $NiCl^+$ and $MnCl^+$ were the sole dominant species for chloride-containing Ni and Mn coordination species, thus, only the thermodynamic parameters for chloride-containing Co coordination species were calculated and studied in detail as shown in Table 1. As can be seen, the enthalpy changes of all Co-containing species are positive, suggesting the endothermic nature of the coordination reactions.

Results and discussion

Leaching of EOL LIBs cathode materials with mixed acids

Pre-treatment of EOL LIBs. The dismantled EOL LIBs went through a pretreatment process for the recovery of cathode powders as shown in Fig. S1 in the ESI.† XRF analysis of as-recovered cathode powders are shown in Table S1 in the ESI,† respectively. The EOL LIBs cathode usually went through a crystalline phase transformation process during the calcination. The *in situ* XRD patterns of the cathode from 100 ~ 800 °C demonstrated the phase transformation process (Fig. 1a). Detailed XRD patterns around the characteristic peaks (18 to 21°) indicated that the crystalline phase transformation started around 300 °C and stabled around 600 °C (Fig. 1b), the deconvoluted XRD patterns around the characteristic peaks at 100 °C (Fig. 1c) and 600 °C (Fig. 1d) showed the predominant phases changed from $Li_{0.9}Co_{1.04}O_2$ and $LiCoO_2$ to $Li_{0.49}CoO_2$, indicating the diffusion of lithium to a third phase at high temperatures, which might facilitate the leaching of lithium from EOL LIBs cathode.

Optimization of leaching conditions. The effect of mixed acid ratios on the leaching efficiencies of strategic metals from EOL LIBs is shown in Fig. 2. Detailed leaching effect data are shown in Table S2 in the ESI,† where other numerical points are fitted by interpolation. As can be seen, the leaching efficiencies with single acid were the lowest among all possible combinations, and the leaching efficiencies orders with single acid are VC > HCl > HNO_3 for Co (Fig. 2b) and HCl > VC > HNO_3 for Li (Fig. 2a), Ni (Fig. 2c), and Mn (Fig. 2d). While the leaching efficiencies with mixed acids were better than those of single or two acids, and the highest leaching efficiencies for each metal were achieved with 0.5 M HCl, 0.25 M HNO_3, and 0.25 M VC. The leaching kinetics of Co with various combinations of acids are shown in Fig. S2 in the ESI.†

Correlation and significance adopted from statistics were utilized to quantitatively describe the association between mixed acids ratios and leaching efficiencies (Fig. S3a in the ESI†). All acids ratios show strong positive correlations (PCC > 0) with the leaching efficiencies, and a clear decrease of PCC was observed with the increase of HCl ratios in the mixture until $HCl : HNO_3 : VC = 2 : 1 : 1$ (PCC = 0.774), suggesting the increase of HCl in the mixture is in favor of a higher leaching efficiency, followed by a rapid increase to PPC = 0.893 with pure HCl. While the significance went through a different process, which first increased from 0.085 at $HCl : HNO_3 : VC = 0 : 1 : 0$ to 0.124 at $HCl : HNO_3 : VC = 2 : 1 : 1$, suggesting a wider distribution of leaching efficiencies with time, and then decreased to 0.042. The correlation and significance results verified the leaching efficiencies shown in Fig. 2. Eh-pH diagram (Fig. S3b in the ESI†) suggested fast leaching kinetics in the first 10 min, with a rapid decrease of Eh and increase of pH caused by the

Table 1 Thermodynamic parameters of the Co-containing coordination species with inorganic ligands

Coordination species	ΔH^0	ΔS^0	90 °C		70 °C		50 °C		30 °C	
	kJ mol^{-1}	J (mol·K)$^{-1}$	ΔG	log K	ΔG	log K	ΔG	log K	ΔG	log K
$CoCl^+$	24.6	81.9	−5.12	0.74	−3.48	0.53	−1.84	0.30	−0.198	0.03
$CoCl_2$	73.8	210	−2.62	0.38	1.59	−0.24	5.81	−0.94	10.0	−1.73
$CoCl_3^-$	113	314	−0.392	0.06	5.89	−0.90	12.2	−1.97	18.5	−3.18
$CoCl_4^{2-}$	118	350	−8.88	1.28	−1.87	0.28	5.14	−0.83	12.2	−2.10
$CoNO_3^+$	19.6	68.9	−5.36	0.77	−3.98	0.61	−2.60	0.42	−1.22	0.21
$CoNO_2^+$	29.9	120	−13.8	1.98	−11.4	1.73	−8.97	1.45	−6.55	1.13

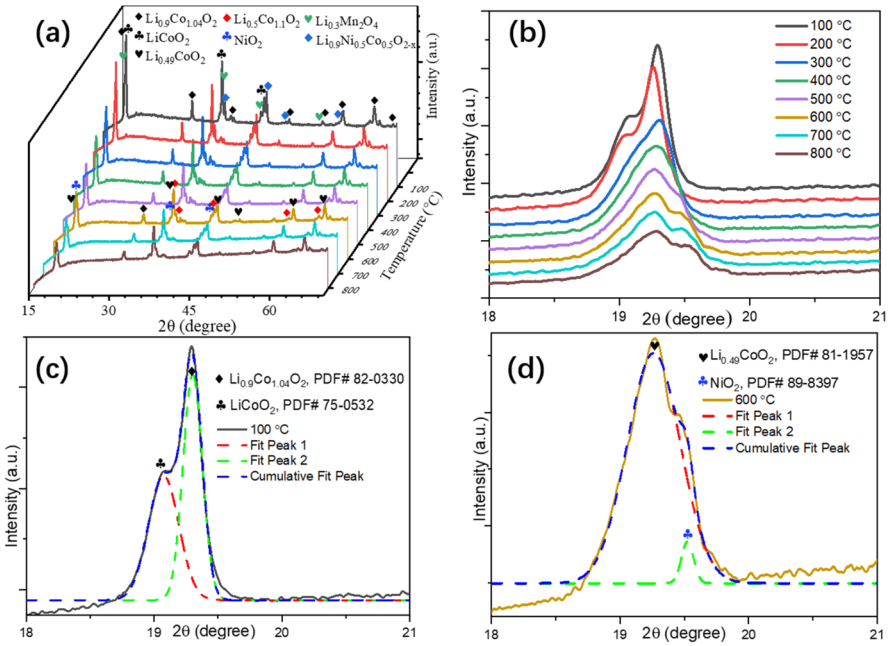

Fig. 1 *In situ* XRD patterns of EOL LIBs cathode powders (a), *in situ* XRD patterns around the characteristic peaks (b), and the deconvoluted XRD patterns around the characteristic peaks at 100 °C (c) and 600 °C (d).

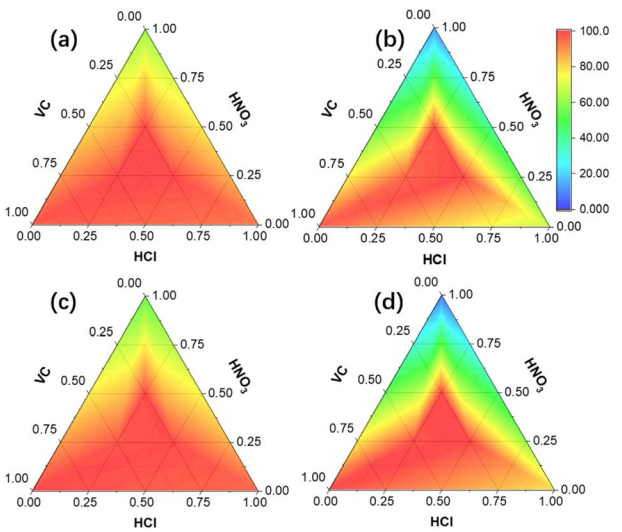

Fig. 2 Leaching efficiency distributions of Li (a), Co (b), Ni (c), and Mn (d) with various acids ratios at 40 min and 10 g L^{-1} solid–liquid ratio.

rapid dissolution of crystal structures, then both values stables around 40 min with final pH of 0.815 and Eh of −206.3 mV.

With the optimal leaching acids ratios, the effect of leaching temperature on the leaching kinetics of strategic metals was studied (Fig. S4 in the ESI†). The leaching kinetics of Li, Ni, and Mn were faster than those of Co's at all temperatures, with Li owning the fastest kinetics among all strategic metals. The fast leaching kinetics of Li might be related to the diffusion of Li to a third phase shown in Fig. 1. A clear increase of leaching kinetics with the increase of temperature was observed, with 82.71% Co leached at 30 °C (Fig. S4a in the ESI†) and 99.98% Co leached at 90 °C (Fig. S4d in the ESI†). Also, a two-stage leaching process was observed, *i.e.*, a fast-leaching process in the first 10 min, which corresponds to the Eh-pH diagram shown in Fig. S3b in the ESI,† and slow leaching kinetics afterward. The highest leaching efficiencies are achieved with 0.5 M HCl, 0.25 M HNO_3, 0.25 M VC, 90 °C, 10 g L^{-1} solid–liquid ratio, 40 min as shown in Table S2 in the ESI.† A feasible, high efficiency (99.98% Co, 99.98% Ni, 99.99% Mn, and 99.99% Li), and ultra-fast leaching of EOL LIBs cathode were achieved. The mixed acid leaching system, not only increased the leaching efficiencies of strategic metals from EOL LIBs cathode materials but also decreased the consumption of VC by half.[4,22]

Evaluation of the leached residual. The leached residual was then analysed with SEM-EDX (Fig. S5 in the ESI†). Only impurities, *i.e.*, Al, O, C and F, were detected in the leaching residual, indicating the completely leaching of strategic metals from EOL LIBs cathode materials. To study the existential status of strategic metals and impurities in the residual (Fig. S6 in the ESI†), XPS analysis of the leached residual at 30 °C was carried out. Co, O, and Al are the majority elements left in the residual (Fig. S6a in the ESI†). Deconvoluted high-resolution curves of Co (Fig. S6b in the ESI†) shows that $2p_{3/2}$ orbitals at 779.3 eV and 780.3 eV were attributed to Co_3O_4 and CoO, respectively, while the $2p_{1/2}$ orbitals at 794.6 eV and 795.9 eV were both attributed to Co_3O_4, indicating two different existential statuses of Co in the leached residual. The existence of CoO and Co_3O_4 was also confirmed with the deconvoluted high-resolution curve of O (Fig. S6c in the ESI†), with O 1s orbitalis at 530.4 eV and 529.35 eV, respectively. And another peak at 531.15 eV was also found on O 1s orbital, suggesting the existence of Al_2O_3 in the residual. The Al 2p and $2p_{3/2}$

orbitalis at 71.1 eV and 74.1 eV both correspond to Al_2O_3, which verified the existence of Al_2O_3 in the residual (Fig. S6d in the ESI†). Detailed binding energy (E_b), full width at half maximum intensity (FWHM), integrated area data are shown in Table S3 in the ESI.†

Leaching thermodynamics. The sole chloride-containing Ni (Fig. S7a in the ESI†) and Mn (Fig. S7b in the ESI†) dominant species in the experimental temperature and pH range were $NiCl^+$ and $MnCl^+$, respectively. And the dominant coordination species in the leaching solution were $NiNO_3^+$, $NiCl^+$, and $MnCl^+$. Since the dominant transition metal in the cathode power is Co, only the thermodynamic parameters of Co are calculated in detail. Thermodynamic calculations suggested four Co-containing species predominate the whole pH range at 30 °C (Fig. 3a), *i.e.*, Co^{2+}, $CoCl^+$, $CoNO_2^+$ and $Co(OH)_2$(s), the chloride complex species with more coordination numbers were not concentrated enough to become the dominant species due to the negative stability constants.[25,26] And with the increase of temperature, more coordination species started to appear, *i.e.*, $CoNO_3^+$ at $T \geq 50$ °C (Fig. 3b, c, and d) and $CoCl_4^{2-}$ at 90 °C (Fig. 3d), accompanied by the increase of coordination species. Since the leaching process took place within the pH range of 0.3 to 0.9 (Fig. S3b in the ESI†), thus, the species distributions within that range are of great importance to the leaching mechanism. The faction of Co^{2+} decreased from around 90% at 30 °C to 83% at 50 °C and further decreased to 73% at 70 °C and finally decreased to 59% at 90 °C. The reaction equations for the leaching process can then be written as eqn (10)–(14).

$$2LiCoO_2 + C_6H_8O_6 + 6H^+ \Leftrightarrow 2Li^+ + 2Co^{2+} + C_6H_6O_6 + 4H_2O \quad (10)$$

$$NO_3^+ + C_6H_8O_6 \Leftrightarrow NO_2^+ + C_6H_6O_6 + H_2O \quad (11)$$

$$C_6H_6O_6 + H_2O \Leftrightarrow C_6H_8O_7 \quad (12)$$

$$2Co_2^+ + 5Cl^- \overset{\Delta}{\rightleftharpoons} CoCl^- + CoCl^{4-} \quad (13)$$

$$2Co^{2+} + NO_3^- + NO_2^- \overset{\Delta}{\rightleftharpoons} CoNO_3^+ + CoNO_2^+ \quad (14)$$

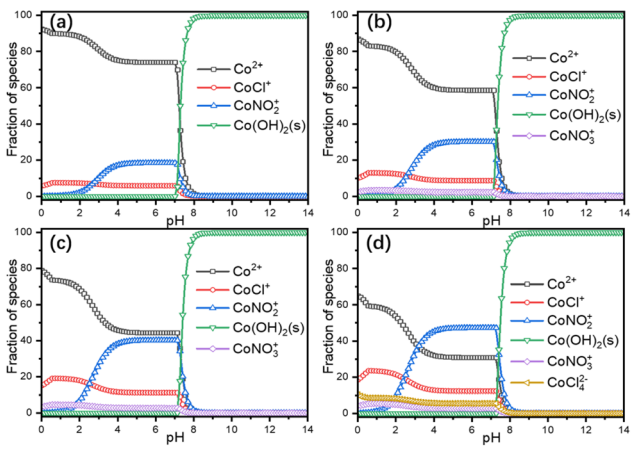

Fig. 3 Thermodynamic calculations of Co-containing species at 30 °C (a), 50 °C (b), 70 °C (c) and 90 °C (d).

The leaching started with the reduction and decomposition of the crystal structure according to eqn (10), meanwhile, nitrate ions could also be reduced by VC to form nitrite ions as shown in eqn (11), then the oxidized dehydroascorbic acid (DHA) went through a hydration process according to eqn (12), generating bicyclo-dehydroascorbic acid (Bi-DHA, detailed structure shown in Fig. S8 in the ESI†). Then, the dissolved Co^{2+} could form coordination species with chloride (eqn (13)) and nitrate/nitrite ions (eqn (14)). Detailed species distributions including minority species are shown in Fig. S9 in the ESI.†

The formation of coordination species was verified with the UV-vis spectrum (Fig. S10 in the ESI†). The hypsochromic shift observed in mixed solution at 0 min (Fig. S10a in the ESI†) compared with that in pure VC solution was caused by the suppressed VC dissociation in strong proton donor solution. A clear decrease of absorbance with time indicates a rapid consumption of VC (Fig. S10b in the ESI†), especially in the first 10 min. The deconvoluted absorbance curves at 1 min (Fig. S10c in the ESI†) and 40 min (Fig. S10d in the ESI†) show that absorbance was mainly caused by the chloride ions (green line) and coordination species with Co (red line). And the hypsochromic shift was also observed, with $\lambda_{max1} = 243.7$ nm at 1 min and $\lambda_{max1} = 242.97$ nm at 40 min (deconvoluted curves at 5, 7, 11, and 20 min are shown in Fig. S11 in the ESI†), which suggested a decrease of coordination numbers with the increase of leaching time.

More comprehensive kinetic models (Table S7 in the ESI†) were utilized to determine the rate-controlling step in the leaching process. The kinetic models with the optimal regression *R*-Square are shown in Fig. 4. The controlled steps for the leaching of Li (Fig. 4a) and Co (Fig. 4b) are in accordance with the exponential law and Prout-Tompkins model, respectively, while both Ni (Fig. 4c) and Mn (Fig. 4d) are diffusion-controlled (Dickinson and Heal model). By fitting $-\ln k$ *vs.* $1000/T$, the apparent activation energy (E_a) can also be calculated according to eqn (15).

$$-\ln k = (E_a/R)T - \ln A \quad (15)$$

where k is the rate constant, A is the pre-exponential factor, E_a is the apparent activation energy, T is the temperature in K. The calculated E_a for the leaching of Li, Co, (Fig. 4e) Ni, and Mn (Fig. 4f) is 22.58 kJ mol^{-1}, 3.366 kJ mol^{-1}, 15.74 kJ mol^{-1}, and 18.55 kJ mol^{-1}, respectively, which are significantly lower than previously reported results.[18] A small E_a might lead to fast leaching kinetics as shown in Fig. S4 in the ESI.† Detailed fitting parameters are shown in Table S5 in the ESI.†

Precipitation of $Al(OH)_3$ and Li_2CO_3

The effluent from the leaching process contains both strategic metals and impurity, *i.e.*, Li^+, Co^{2+}, Ni^{2+}, Mn^{2+}, Al^{3+}. To narrow down the experimental range and comprehend the precipitation mechanism, all leached elements and corresponding chemical reactions were considered in the thermodynamic calculations (Fig. 5a). With the addition of NH_4OH, And the experimental results (Fig. 5b) suggested the optimum pH being 5.5 with 98.5% Al^{3+}, 3.1% Co^{2+}, 4.7% Ni^{2+}, 3.3% Mn^{2+} and 4.5%

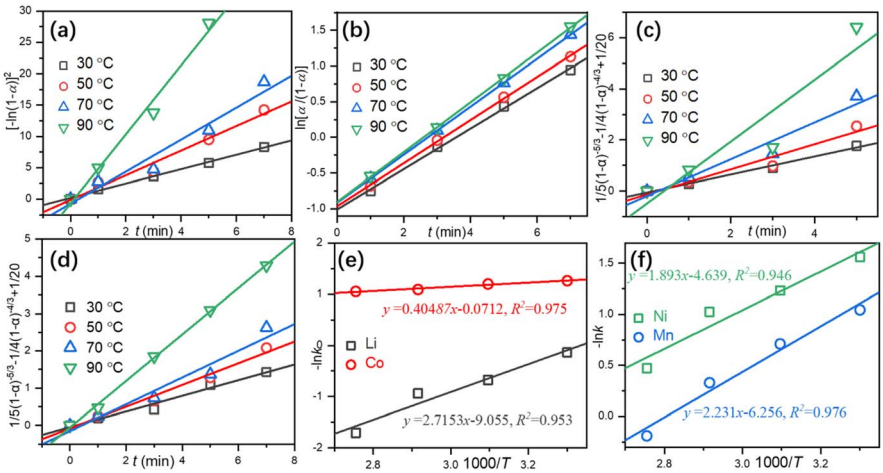

Fig. 4 Linear regressions of Li (a), Co (b), Ni (c), and Mn (d) and a plot of $-\ln k$ *vs.* $1000/T$ for Li, Co, (e) Ni and Mn (f).

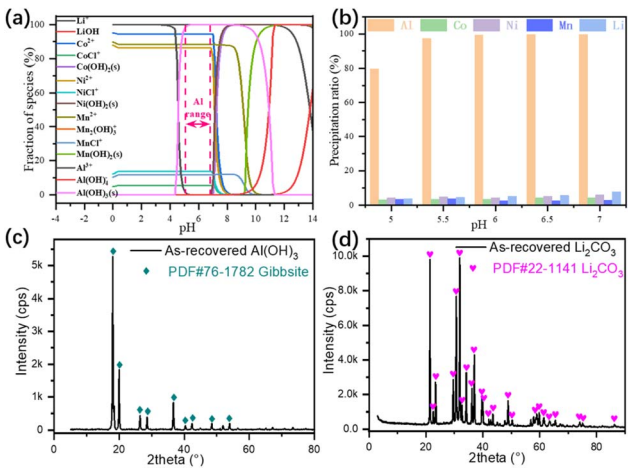

Fig. 5 Thermodynamic calculations of the leached species for aluminum precipitation (a), experimental results in the pH range of 5 to 7 for the precipitation of $Al(OH)_3$ (b), XRD pattern of the precipitated $Al(OH)_3$ (c), and Li_2CO_3 (d).

Li^+ precipitated.[32] The loss of strategic metals, especially Li^+, in the precipitation process was caused by the adsorption between the layered double hydroxide structure of $Al(OH)_3$. XRD pattern of the as-recovered sediment at pH 5.5 (Fig. 5c) indicates that the dominant phase was gibbsite.[33] The effluent from the NCM622 precursor precipitation process was concentrated to obtain a higher Li^+ precipitation ratio. The XRD pattern of the as-recovered Li_2CO_3 (Fig. 5d) suggested a high degree of crystallinity, thus the as-recovered Li_2CO_3 is suitable for the remanufacturing of cathode materials.

Preparation and electrochemical performance of NCM622 cathode material

The effluent from the impurity removing step cannot be directly used for the manufacturing of NCM622 precursor, due to the lack of nickel and manganese, thus external nickel and manganese source is needed. After adjusting the ratio of Ni^{2+}, Co^{2+}, and Mn^{2+}, the solution is ready for the precipitation of the NCM622 precursor. The concentration of each metal ion in the leaching solution and the metal molar ratio after adjustment is shown in Table S1.† Thermodynamic calculations were also conducted (Fig. 6a), and the initial pH where Ni^{2+}, Co^{2+}, and Mn^{2+} started to precipitate was significantly reduced due to the addition of Na_2CO_3. The NCM622 precursor precipitation pH range was 6 to 10 since lower pH might result in incomplete precipitation while higher pH would facilitate the existence of metal hydroxides. Based on this, the NCM622 precursor precipitation experiments were carried out at pH 6 to 10 (Fig. 6b). A clear increase of precipitation ratios was observed with the increase of pH and the optimum condition for NCM622 precursor precipitation was pH 8. SEM-EDX (Fig. S12 in the ESI†) images of the as-recovered NCM622 precursor demonstrated a smooth, porous, and spherical-like morphological with Ni^{2+}, Co^{2+}, and Mn^{2+} evenly distributed on the surface.

The NCM622 cathode material was obtained by calcining the mixture of NCM622 precursor and Li_2CO_3 under an oxidization atmosphere. XRD pattern of the as-recovered NCM622 cathode material (Fig. 6C) indicated the cathode material possesses a hexagonal α–$NaFeO_2$ structure with a space group of $R\bar{3}m$, which verified the dominance of the NCM622 phase in the mixture. The detailed crystal lattice structure parameters shown in Table S9 in the ESI† suggested a well-ordered layered hexagonal structure with a low degree of Li^+/Ni^{2+} mixing ratio, which would facilitate the diffusion of Li^+ in the cathode material. The first charge and discharge capacities (Fig. 6d) of the NCM622 cathode material were 193.9 mA h g^{-1} and 163.7 mA h g^{-1}, respectively, and a similar charge and discharge curves were also observed in the following two cycles, indicating a high capacity of the remanufactured cathode material. The initial coulombic efficiency of NCM622 cathode material is 84.42%. The cyclic voltammetry test of the prepared NCM622 cathode material was carried out after three charge–discharge cycle tests. CV curves (Fig. 6e) of the NCM622 cathode material show one pair of redox peaks with an anodic peak potential E_{pa} = 3.759 V, anodic peak current i_{pa} = 0.3862 mA, cathodic peak

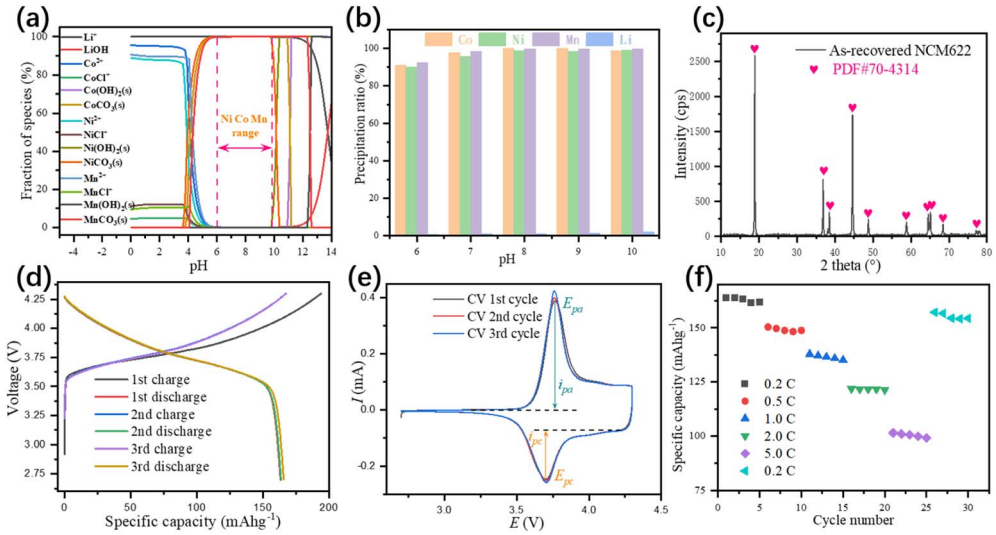

Fig. 6 Thermodynamic calculations of the leached species for NCM622 precursor precipitation (a), experimental results in the pH range of 6 to 10 (b), XRD pattern (c), charge–discharge curves (d), CV (e), and rate performance (f) of the as-recovered NCM622 cathode material.

potential $E_{pc} = 3.721$ V, and cathodic peak current $i_{pc} = -0.1730$ mA, respectively. The relatively low peak potential difference $\Delta E = 0.038$ V indicates a reliable reversible capacity and low polarization of the NCM622 cathode material, while the asymmetric peak currents were caused by the lithium metal anode. The rate capabilities (Fig. 6f) of the NCM622 cathode material were tested 5 times at 0.2C, 0.5C, 1.0C, 2.0C, 5.0C, and finally 0.2C again. The initial discharge capacities were 163.8 mA h g^{-1}, 150.4 mA h g^{-1}, 137.8 mA h g^{-1}, 121.9 mA h g^{-1}, 101.5 mA h g^{-1}, and 157.2 mA h g^{-1}, respectively, at different rates. The capacity retention of NCM622 was 94.3% with a capacity of 154.4 mA h g^{-1} after 30 cycles at different rates, which indicates a low polarization and stable layered structure of the NCM622 cathode material.

Conclusions

A closed-loop hydrometallurgy recycling process for the recycling of EOL LIBs cathode materials was developed to manufacture NCM622 cathode materials. Thermodynamic calculations were proven effective for both determining the experimental range and interpreting the mechanism. Based on the thermodynamic calculations and kinetic regressions, the synergy-enhanced leaching mechanism in the HCl-HNO_3-VC leaching system was revealed. The leaching started with the diffusion of reactants to the solid–liquid boundaries, where reduction reaction takes place and the controlled step for Co are crystal decomposition (Prout–Tompkins model), generating reduced strategic metal ions. Then, the strategic metals diffuse through the diffusion layer into bulk solution, where anion ions coordinate with transition metals, especially Co, forming stable coordination species. The formation of coordination species lowers the system energy, thus, leading to the reduction of the apparent activation energy, which in return facilitates fast leaching kinetics in the system. The Ni-rich NCM622 cathode material manufactured from EOL cellphones and laptops LIBs demonstrated excellent electrochemical reversibility ($\Delta E = 0.038$ V), low polarization, high rate capabilities (163.8 mA h g^{-1}), and capacity retention ratio (94.3%).

Conflicts of interest

There are no conflicts to declare.

Acknowledgements

This research was sponsored by the Shanghai Sailing Program (Grant number 21YF1409000), Nature Science Foundation of Shanghai (Grant number 22ZR1415800).

References

1 Y. Chen, N. Liu, F. Hu, L. Ye, Y. Xi and S. Yang, *Waste Manage.*, 2018, **75**, 469–476.
2 M. Chen, X. Ma, B. Chen, R. Arsenault, P. Karlson, N. Simon and Y. Wang, *Joule*, 2019, **3**, 2622–2646.
3 G. Harper, R. Sommerville, E. Kendrick, L. Driscoll, P. Slater, R. Stolkin, A. Walton, P. Christensen, O. Heidrich, S. Lambert, A. Abbott, K. Ryder, L. Gaines and P. Anderson, *Nature*, 2019, **575**, 75–86.
4 L. Xing, J. Bao, S. Zhou, Y. Qiu, H. Sun, S. Gu and J. Yu, *Chem. Eng. J.*, 2021, **420**, 129593.
5 W. Chu, Y. L. Zhang, X. Chen, Y. G. Huang, H. Y. Cui, M. Wang and J. Wang, *J. Power Sources*, 2020, **449**, 227567.
6 X. Chen, J. Li, D. Kang, T. Zhou and H. Ma, *Green Chem.*, 2019, **21**, 6342–6352.
7 E. Gratz, Q. Sa, D. Apelian and Y. Wang, *J. Power Sources*, 2014, **262**, 255–262.
8 S. P. Barik, G. Prabaharan and L. Kumar, *J. Cleaner Prod.*, 2017, **147**, 37–43.

9 W. Gao, C. Liu, H. Cao, X. Zheng, X. Lin, H. Wang, Y. Zhang and Z. Sun, *Waste Manage.*, 2018, **75**, 477–485.

10 C. H. Jo and S. T. Myung, *J. Power Sources*, 2019, **426**, 259–265.

11 P. Meshram, B. D. Pandey and T. R. Mankhand, *Chem. Eng. J.*, 2015, **281**, 418–427.

12 S. M. Shin, N. H. Kim, J. S. Sohn, D. H. Yang and Y. H. Kim, *Hydrometallurgy*, 2005, **79**, 172–181.

13 G. Gao, X. Luo, X. Lou, Y. Guo, R. Su, J. Guan, Y. Li, H. Yuan, J. Dai and Z. Jiao, *J. Mater. Cycles Waste Manage.*, 2019, **21**, 942–949.

14 X. Zeng, J. Li and B. Shen, *J. Hazard. Mater.*, 2015, **295**, 112–118.

15 L. Li, J. Ge, R. Chen, F. Wu, S. Chen and X. Zhang, *Waste Manage.*, 2010, **30**, 2615–2621.

16 X. Chen, D. Kang, J. Li, T. Zhou and H. Ma, *J. Hazard. Mater.*, 2020, **389**, 121887.

17 Q. Meng, Y. Zhang and P. Dong, *Waste Manage.*, 2017, **64**, 214–218.

18 Y. Zhang, Q. Meng, P. Dong, J. Duan and Y. Lin, *J. Ind. Eng. Chem.*, 2018, **66**, 86–93.

19 L. Li, J. Lu, Y. Ren, X. X. Zhang, R. J. Chen, F. Wu and K. Amine, *J. Power Sources*, 2012, **218**, 21–27.

20 J. Wang, K. Huang, H. Dong, Y. Lu, K. Liu, Z. Chen, X. Shan, G. Huang and L. Wei, *RSC Adv.*, 2022, **12**, 23683.

21 M. Xu, S. Kang, F. Jiang, X. Yan, Z. Zhu, Q. Zhao, Y. Teng and Y. Wang, *RSC Adv.*, 2021, **11**, 27689.

22 S. Gu, L. Zhang, B. Fu, J. W. Ahn and X. Wang, *J. Cleaner Prod.*, 2020, **266**, 121827.

23 H. Chen, S. Gu, Y. Guo, X. Dai, L. Zeng, K. Wang, C. He, G. Dodbiba, Y. Wei and T. Fujita, *Hydrometallurgy*, 2021, **205**, 105746.

24 S. Gu, B. Fu, T. Fujita and J. W. Ahn, *Appl. Sci.*, 2019, **9**(11), 2262.

25 A. A. Migdisov, D. Zezin and A. E. Williams-Jones, *Geochim. Cosmochim. Acta*, 2011, **75**, 4065–4079.

26 W. Liu, S. J. Borg, D. Testemale, B. Etschmann, J. L. Hazemann and J. Brugger, *Geochim. Cosmochim. Acta*, 2011, **75**, 1227–1248.

27 C. Hopa, R. Kurtaran, E. Hopa, G. Cetin, E. Dundar, H. Kara and M. Alkan, *Inorg. Chim. Acta*, 2015, **429**, 15–21.

28 H. Yokoyama, A. Masuno, M. Misoo, K. Yamaguchi and S. Suzuki, *J. Coord. Chem.*, 2010, **63**, 762–775.

29 D. M. L. Goodgame and M. A. Hitchman, *Inorg. Chem.*, 1965, **4**, 721–725.

30 H. Suzuki, M. Koide and S. I. Ishiguro, *J. Chem. Soc., Faraday Trans.*, 1993, **89**, 3055–3060.

31 O. M. Suleimenov and T. M. Seward, *Chem. Geol.*, 2000, **167**, 177–192.

32 X. Yang, Y. Zhang, Q. Meng, P. Dong, P. Ning and Q. Li, *RSC Adv.*, 2021, **11**, 268.

33 S. Gu, L. Zhang, B. Fu, X. Wang and J. W. Ahn, *Chem. Eng. J.*, 2021, **420**, 127561.